

Cancer Immunotherapy Based on Carbon-Quantum-Dot Modified Cancer Cells

Zikang Tang (✉ zktang@um.edu.mo)

University of Macau <https://orcid.org/0000-0001-9998-4940>

Tao Liang

University of Macau

Josh Haipeng Lei

University of Macau

Jinsong Tao

University of Macau

Sen Guo

University of Macau <https://orcid.org/0000-0002-2681-0576>

Hanlu Gao

University of Macau

Lipeng Zhu

University of Macau

Yinning Zhou

University of Macau

Youcheng Liu

University of Macau

Long Xi

University of Macau

Haibo Tong

University of Macau

Enshan Liu

University of Macau

Bohan Zhang

University of Macau

Heng Sun

University of Macau

Huiqi Zhang

University of Macau

Kathy Qian Luo

University of Macau

Qi Zhao

University of Macau

Tzu-Ming Liu

University of Macau

Defang Ouyang

University of Macau

Wei Ge

University of Macau

Ying Zheng

University of Macau

Chuxia Deng

University of Macau

Songnan Qu

University of Macau

Biological Sciences - Article

Keywords:

Posted Date: April 26th, 2021

DOI: <https://doi.org/10.21203/rs.3.rs-457550/v1>

License:   This work is licensed under a Creative Commons Attribution 4.0 International License.

[Read Full License](#)

Abstract

Cancer immunotherapy based on carbon-quantum-dot (CQD) modified cancer cells (CM-cancer) has proven effective. The CQDs non-distinctively modify the conformational structure of proteins by hydrogen bonding between the protein chains and the permeated CQDs via a thermal treatment. CM-cancer vaccines exhibit robust immunogenicity, which can recruit macrophages and dendritic cells to effectively deliver the cancer antigens into lymph nodes to activate CD8⁺ T cells, and eventually leads to an anti-cancer immune response all over the body. The CM-cancer vaccinations are not only able to inhibit primary tumors, but also clearly eliminate metastatic tumors. Our research demonstrates a promising personalized cancer immunotherapeutic technology for potential clinical applications.

Introduction

Cancer is one of the leading causes of death in the world. It is the central research topic on cancer immunotherapy via training the immune system to recognize cancer-specific antigens (neoantigens) following up to kill the cancer cells and overcome cancer recurrence and metastasis. Cancer cells exhibit highly distinct compositions of mutation with limited overlapping similarities among patients^{1,2}. Personalized cancer vaccines are vigorously developed vaccine strategies that aim to modulate the innate and adaptive immune systems for activating anticancer immunity with neoantigens³⁻⁵. Although recent progresses in massive parallel sequencing as well as machine learning make cancer vaccine more feasible, efficient screening and identifying neoantigens for patients is still challenging. A full course of the identification process is high cost and time consuming.^{6,7} Furthermore, cancer vaccines that target multiple neoantigens are considered more effective than targeting a single neoantigen⁸⁻⁹. However, it is extremely challenging to design and produce personalized multi-targeted cancer vaccines within a reasonable short preparation time at affordable cost to serve ordinary cancer patients. Herein, we reported a novel route of cancer immunotherapy based on modification of cancer cells by carbon-quantum-dots (CQDs). We found that the CQDs can non-distinctively modify the conformational structure of proteins through a facile thermal treatment. Vaccination with CQD-modified cancer cells (CM-cancer) can recruit macrophages (MPs) as well as dendritic cells (DCs) to effectively deliver the cancer antigens into lymph nodes and eventually leads to specific anti-cancer immune response for the whole body. The CM-cancer vaccinations are not only able to inhibit primary tumors, but also clearly eliminate metastatic tumors. In this process, the extremely troublesome and time-consuming neoantigen identification are smartly avoided and passed it to antigen presentation cells (APCs) like MPs or DCs, which are of distinct and incomparable advantages for customized cancer immunotherapy. The thermal induced non-distinctive modification of proteins by CQDs paves the way for personalized cancer immunotherapy.

Cancer cells are a natural source for multiple cancer neoantigens, including those not yet identified¹⁰. However, a whole-cancer-cell vaccination always lacks robust immune stimulation, and limited anti-cancer responses¹¹. The primary reasons for this may attributed to most contained proteins in cancer cells being self-body proteins, which have very low immunogenicity, and express weak “eat me” signal to

APCs. Derived from normal cells variations, the cancer cells contain multiple immune inhibitory proteins, such as CD24, CD31, CD47, which express “don’t eat me” signal to prevent self-body phagocytosis^{12–15}. All these lead to low cellular uptake efficiency of the neoantigens by APCs, and their inefficient accumulation in lymphatic nodes result in the non-effective anti-cancer T-cell activation. In recent advances, many strategies were proposed to enhance the immunogenicity of the cancer cells by coupling with adjuvant or blocking the immune inhibitory proteins on cancer cells^{16–19}. However, these methods cannot inherently change or enhance the immunogenicity of the cancer cells in large extent. To achieve satisfied anti-cancer immunotherapy, immune checkpoint blockade (ICB) reagents are then commonly adopted in combination^{20–22}.

CQDs are promising biomedical materials due to their super small size (<10 nm), excellent biocompatibility and non-toxicity^{23–25}. Via a thermal treatment, the ultra-small CQDs modify the conformational structure of proteins without distinction through hydrogen bonds between the CQDs and protein chains. These conformational modifications lead to a significant enhancement in immunogenicity meanwhile dysfunction the immune inhibitory proteins on cancer cells. In vitro, the CM-cancer vaccine hyperactivate MPs with enhanced cellular uptake efficiency and increased MHC-II expression. In vivo, the CM-cancer vaccine robustly triggers immune response to recruit MPs and DCs, then engulf and deliver the cancer antigens into the lymph nodes to activate CD8⁺ T cells, eliciting a powerful whole body anti-cancer immune response. Furthermore, we also demonstrate that vaccination with CM-4T1 not only inhibit the primary tumors and prevent from metastasis, but also eliminate the metastatic tumors in the post-surgical 4T1 cancer model with excellent prognosis.

Results

Synthesis and characterization of CQDs modified proteins

To awaken the immune system precisely functioning to cancers, a potential solution is to change the conformational structures of the self-body proteins on the cancer cell surface to enhance the “eat me” signal and weaken the “don’t eat me” signal simultaneously.^{12–15} Unfortunately, researchers have suffered from laboursome and troublesome procedures based on current precise protein modification strategies to achieve these goals. Instead, we developed a facile CQD-based technology which can modify a batch of proteins’ conformational structures without species and amount limitation.

The CQDs were synthesized from a classical dehydration and carbonization process from citric acid and urea via a solvothermal route^{23–26}. In this procedure, 4A molecular sieve was added to increase the dehydration process between citric acid and urea. As shown in the transmission electron microscope (TEM) image (Fig. 1a), the diameters of the CQDs range from 2 nm to 5 nm with clear 0.21 nm lattice fringes, which corresponds to (100) plane of graphite. The heights of the CQDs range from 2 nm to 5 nm as shown in the atomic force microscope (AFM) image (Fig. 1b). The elemental compositions of the CQDs are revealed by energy-dispersive X-ray spectroscopy (EDS) profiles, which demonstrates the presence of C, O, N, and S elements (Supplementary Fig. 1). The CQDs aqueous solution exhibits main

absorption peaks at 600 and 665 nm, and a weak deep-red emission peak at 715 nm under the 665 nm laser excitation (Fig. 1c).

To analyze how the CQDs affect the protein conformational structures, we took one classic protein of bovine serum albumin (BSA) as an example. Upon mixing with BSA at room temperature, the deep-red emission from the CQDs was enhanced accompanying with 10 nm blue shifted (Fig. 1c). After annealed at a temperature above 50 °C for 10 min and then naturally cooled down to room temperature, the deep-red emission from the CQDs were significantly enhanced, while its absorption spectrum was nearly unchanged. Obviously, the annealing process combined the CQDs and BSA together, which prevented the fluorescence quenching by water molecules. SDS-polyacrylamide gel electrophoresis (SDS-PAGE) was further conducted to examine the composition of CQDs and BSA after different temperatures annealing. As comparison, significant enhanced emission band could be observed in the samples after annealed at the temperature above 50 °C (Fig. 1d), in consistent with their Coomassie Brilliant Blue staining band areas (Supplementary Fig. 2). We took 50 °C annealing treatment to produce the CQDs and proteins or cells composites, which were named with CM-protein or CM-cell. As shown in Fig. 1e, all the proteins band areas exhibited obvious red fluorescence in the annealed *Fgfr2-S252W* tumors whole proteins (WPs) with CQDs (CM-WP), while no clear fluorescence were observed in proteins band areas of the WPs with CQDs without annealing (Supplementary Fig. 3). These phenomena could be further visualized in fluorescence imaging observation in vitro. We found that the CQDs could not be actively ingested by living cells or stably bonded to cell surfaces at the body temperature, as confirmed by no clear red fluorescence of the cells co-incubated with the CQDs for 24 h (Supplementary Fig. 4). In contrast, obvious red fluorescence was observed in the cells co-incubated with the CQDs after annealing at above 50 °C for 10 mins (Supplementary Fig. 5). The confocal laser scanning microscopy (CLSM) image with red fluorescent signal of a single CM-4T1 further evidenced the thermal-induced composition of CQDs with whole proteins of the cells (Fig. 1f). Similar phenomena could be observed in different cells as well, such as MDA-MB-231, EMT6, 4T1 and *Fgfr2-S252W* cells (Supplementary Fig. 4, 5), implying that thermal induced protein-bonding ability of the CQDs was universal to proteins.

The chemical structure of freeze-dried powder from the CQDs and BSA solutions with and without the annealing, named CM-BSA and CQDs+BSA, respectively, were investigated by means of FTIR spectrometer. As shown in Fig. 1g, an enhanced absorption peak at 3300 cm^{-1} , which corresponded to the stretching vibration of N–H bonds²⁷, was observed in the CM-BSA, indicating the formation of stable complexes through hydrogen bonding between the CQDs and the BSA protein after the annealing. The conformational changes of the BSA protein before and after combining with the CQDs were investigated further by circular dichroism (CD) spectroscopy. As shown in Fig. 1h and Supplementary Fig. 6, while the CQDs did not show CD signal, the pure BSA and the CQDs+BSA solution at room temperature presented similar CD signals, implying that simply mixing with CQDs at room temperature did not affect the protein's secondary structure. Upon the thermal treatment, the CD signal of the BSA decreased its intensity in α -helix and β -sheet²⁸. However, upon cooling down back to room temperature, the CD signal mostly recovered in the pure BSA but not in the CM-BSA, implying that the annealing process induced an

irreversible remodification in the conformational structure of the CM-BSA through the newly formed hydrogen bonds between the CQDs and the BSA.

To understand the interactions between the CQDs and protein structures in molecular level, we conducted a Molecular Dynamics (MD) simulation for a BSA with and without CQDs at temperature of 37 °C and 70 °C, respectively. According to the experiment results, a four-layer CQDs structure was initially built up by using Discovery Studio 2016 Client software (Extended Data Fig. 1). At 37 °C, no remarkable difference was observed in the configurations of BSA with and without adding CQDs. At 70 °C, the configuration of the BSA became dynamically looser, but the loosen structure recovered after temperature cooling down back to 37 °C. When adding three CQDs to the BSA, the configuration of the BSA significantly changed in both secondary and tertiary structures at 70 °C for 100 ns simulation (Fig. 1I), and the configuration change was kept, even when cooled back down to 20 °C. To further understand the interactions between BSA and CQDs, the number of hydrogen bonds between the CQDs and the BSA during 100 ns simulation at 70 °C were analyzed. As shown in Fig. 1J, the number of hydrogen bonds between CQDs and BSA in the last 2 ns simulation was significantly increased in comparison with that in the first 2 ns simulation. The simulation clearly demonstrated that the conformational structure of BSA could not be changed by the CQDs at body temperature, but could be significantly modified upon the annealing through enhanced hydrogen bonding, in consistent with the experimental observation. With the merit of ultra-small sizes and abundant N–H and C=O groups on the surface, the CQDs could permeate into the tiny loosing space of proteins under the thermal treatment to form enhanced hydrogen bonds with the protein chains, which modified the conformational structure without destructing the amino acid sequence (primary structure) of the protein.

CM-cancer induced MPs hyperactivation and anti-cancer immune response

For applications in biomedical and clinical fields, the cytotoxicity of the CQDs was examined in several cell systems. The CQDs did not affect cell viability even with concentrations up to 500 µg/ml, indicating non- or extremely low cytotoxicity (Supplementary Fig. 7). MPs and DCs are potent antigen-presenting cells and they play Crucial roles in the cancer immunotherapy²⁹.

We adopted RAW264.7 (a murine MP cell line), in vitro, to analyze the behaviors of MPs affected, by inactivated cancer cells, CQDs and CM-cancer cells, respectively. As shown in Fig. 2a and Supplementary Fig. 8, after 6 hr co-cultivation with CM-4T1, the RAW264.7 cells not only increased in cell size but also were hyperactivated into dendritic-like morphology³². While no obvious morphological or size changes were observed the RAW264.7 cells cultivated only with phosphate buffered saline (PBS), CQDs, and heat-shocked 4T1 cells (H-4T1, at 50 °C for 10 mins) with DID700 dye labeled (DID700 dye molecules emit fluorescence in 650-750 nm), respectively. According to the CLSM images, the hyperactivated RAW264.7 cells contained some red emissive objects which were from the endocytosed CM-4T1 and their degradation products, while nearly no red fluorescent species were observed in the RAW264.7 cells co-cultivated with CQDs or DID700–labeled H-4T1. Obviously, the CM-4T1 co-cultivated RAW264.7 cells exhibited much stronger phagocytic activity than the inactivated pure H-4T1. Furthermore, flow cytometric

analysis detected much greater up-regulation of MHC Class II expression on the CM-4T1 co-cultivated RAW264.7 cells than that co-cultivated with CQDs or H-4T1 cells (Fig. 2b), indicating stronger antigen-presenting ability of the CM-4T1 hyperactivated RAW264.7 cells.

To visualize the hyperactivated behavior of MPs triggered by the CM-cancer *in vivo*^{33,34}, a *Tg (mpeg1:EGFP)* transgenic zebrafish model whose MPs specifically expressed green fluorescence protein (EGFP)^{35,36} was examined by abdominal injection into the therapy group of (Z0) CQD-modified melanoma B16F10 cells (CM-B16F10), and control groups of (Z1) PBS, (Z2) CQDs, and (Z3) heatshocked B16F10 cells (H-B16F10) with Dil dye labeled (Dil dye molecules emit fluorescence in 555-650 nm), respectively. At the 6th hr. after injection, no significant recruitment of MPs (green) were observed from the control groups of (Z1)-(Z3) (Fig. 2c, Supplementary Fig. 9). In obvious contrast, the zebrafish with abdominal injection of the CM-B16F10 vaccine demonstrated a significant recruitment of MPs, which were well overlapped within the area of red fluorescent signals coming from the injected CM-B16F10 (Fig. 2c). These phenomena indicated that the MPs were successfully recruited to engulf the injected CM-B16F10. At the 24th hr after CM-B16F10 injection, the number of the recruited MPs was significantly decreased, while merged yellow signals overlapped from the MPs (green) and the engulfed CM-B16F10 (red) were observed to drain into the abdominal subcutaneous lymph (Fig. 2c)³⁷.

To visualize the anti-cancer response triggered by the CM-cancer vaccine *in vivo*, the Dil (red fluorescence) labelled B16F10 cancer xenografts were constructed in *Tg (mpeg1:EGFP)* and *Tg (Ick:EGFP)* transgenic zebrafish models, respectively, whose MPs and T cells express green fluorescence³⁸. The CM-B16F10 (~40 cells, 4 nl) were intraperitoneally injected into the 3-day cancer xenograft transgenic zebrafishes. The anti-cancer MPs and T cells response after the CM-B16F10 vaccine injections were observed by CLSM. As shown in Fig. 2d, a number of MPs were firstly recruited to the cancer site and then infiltrated into the cancer after the CM-B16F10 treatment. The activated T cells were then followup recruited to the cancer site, infiltrated into the cancer with merged yellow dots (Fig. 2e). Actions of the T cells attacking the cancer cells were clearly seen in the image, as evidenced by gradual decrease of the cancer sizes in three days after the CM-B16F10 vaccine injection. In contrast, no significant activated T cells were found in the control group (Supplementary Fig. 10).

The CM-cancer vaccine induced anti-cancer effect was further evaluated in a B16F10-C3 cancer xenograft zebrafish model. The B16F10-C3 cell line was generated by transfecting the plasmid DNA of a CFP (donor) / YFP (acceptor) FRET-based (Fluorescence Resonance Energy Transfer) sensor caspase-3 (C3) into the B16F10 cells, which could serve as a monitor of the cancer cell proliferation growth by YFP imaging (green fluorescence) and detect the caspase-3 activation dependent apoptosis by FRET imaging (blue fluorescence)^{39,40}. The vaccinated therapy group of (B0) CM-B16F10-C3 (~40 cells, 4 nl), and the control groups of (B1) PBS (4 nl), (B2) pure CQDs (4 nl, 200 µg/ml), and (B3) heat-shocked B16F10-C3 (H-B16F10-C3) (~40 cells, 4 nl) were intraperitoneally injected into the 3-day B16F10-C3 cancer xenograft A/B wild type zebrafishes, respectively. The cancer growth was monitored by the YFP imaging at predetermined times. As shown in Supplementary Fig. 11 and 12, the therapy group (B0) showed very

significant inhibition of the cancer, in a sharp contrast with those in the control groups of (B1)-(B3). More excitingly, after the CM-B16F10 vaccination, the cancer nearly disappeared on the day 6 and totally disappeared on the day 8, while the cancer growths of the three control groups were uncontrolled, and eventually all zebrafishes died starting from the days 7 to 8 after the cancer plantation. The apoptosis of the xenograft cancer cells in zebrafish was monitored by FRET imaging which has a living indicator by YFP (acceptor) signal (green), and apoptosis indicator by CFP (donor) signal (blue). As shown in Supplementary Fig. 13, we observed that the living cancer cells (green) were proliferating rapidly in the control groups of (B1)-(B3) from the 3rd day to the 6th day and no apoptosis of cancer cells occurred. In contrast, the apoptosis of cancer cells (blue) in the therapy group of (B0) was very obvious in single cell level on the 6th day, which lively visualized the anti-cancer effect triggered by the CM-cancer vaccination.

Transportation and presentation of the CM-cancer vaccine induced immune response in lymph nodes

The transportation of the CM-cancer vaccination to lymph nodes with activation of MPs and DCs, and anti-cancer response were further investigated in a mouse model. The therapy group of (L0) CM-4T1 (CQDs: 200 µg/ml, cells: 1×10^7 /ml, 100 µl), and the control groups of (L1) PBS (pH 7.4, 100 µl), (L2) pure CQDs (CQDs: 200 µg/ml, 100 µl), and (L3) DID700 dye labeled H-4T1 (cells: 1×10^7 /ml, 100 µl) were intraperitoneal injected into the four groups of Balb/c mice, respectively. The mice were sacrificed at different time points (ranging from 4 hr to 24 hr) after the injections, whose inguinal lymph nodes were collected for histological analysis (Fig. 3, Supplementary Fig. 14). In the therapy group (L0), intensive near infrared (NIR) fluorescence signal (from the combined CQDs) was observed just after 4 hr of vaccination, and then the signal was gradually weakened but retained in the lymph node till to 24 hr. In the control group of (L3), no any labeled-dye fluorescence (NIR) was observed in the lymph node within 24hr after injection, implying that the pure H-4T1 could hardly be delivered to the lymph nodes for activating immune system. Predictably, the other two control groups of (L1) and (L2) did not lead any immune response. The experimental fact indicated that the CM-4T1 vaccine could effectively be drained to lymph nodes. To further evaluate the immune response of the CM-cancer vaccine in lymph nodes, 4 µm-thick inguinal lymph nodes tissue sections from the four groups after injection at 4 hr and 24 hr were stained with anti-CD8⁺ (brown), IFN-γ (brown), F4/80 (brown) and CD11c (brown), respectively. At 4 hr after the injection, CD11c, F4/80, IFN-γ, and CD8⁺ expression were obviously increased in the therapy group (L0), indicating activated MPs and DCs could drain to the lymph nodes and effectively activated cytotoxic T cells at about 4 hr after the CM-4T1 vaccination. At 24 hr after injection, the CD11c, F4/80, IFN-γ, and CD8⁺ still retained high expression in the therapy group (L0). During the studying period, only slightly increased expressions of CD11c, F4/80 and CD8⁺ were observed in the L3 groups at 24 hr after H-4T1 vaccination. All these results demonstrated that vaccination with CM-cancer could effectively recruit and hyperactivate MPs and DCs. By engulfing the CM-cancer, the delivery of cancer antigens were greatly enhanced to lymph nodes and triggered robust cytotoxic T cells response, which was in an obvious contrast with the heat-shocked pure cancer cells vaccination. Noted that for the pure CQDs group, we also observed the delivering of CQDs to lymph nodes, as evidenced by the NIR fluorescence from CQDs which reached to the maximum intensity at around 2 hr. After that, the NIR fluorescence gradually lost its

intensity, and eventually vanished at 24 hr, implying the totally clearance of CQDs out of body. Different from the CM-4T1 vaccine, however, the pure CQDs did not trigger anti-cancer immune response.

CM-cancer vaccines induced specific cancer immunotherapy

To further study the immune response and immunotherapy effect of the CM-cancer vaccines, vaccination protocols of CM-cancer were designed on two murine tumor models, which were 545 cells (Brca1-deficiency tumor cells) in FVB mice and 4T1 in Balb/c mice, as shown in Fig. 4a. Allograft tumors were established by implanting 545 cells (5×10^5 cells) and 4T1 cells (5×10^5 cells) into the 4th mammary fad pads of a normal female FVB and Balb/c mice, respectively. We studied the vaccination effect on the therapy group of (P0) with intraperitoneal injection of the CM-545 and CM-4T1 vaccines (CQDs: 200 $\mu\text{g}/\text{ml}$, cells: $1 \times 10^7/\text{ml}$, 200 μl) in the corresponding murine tumor model in comparison with those control groups by injecting: (P1) PBS (pH 7.4, 200 μl), (P2) pure CQDs (200 $\mu\text{g}/\text{ml}$, 200 μl), (P3) H-545 or H-4T1 (cells: $1 \times 10^7/\text{ml}$, 200 μl), and (P4) CM-EMT6 (CQDs: 200 $\mu\text{g}/\text{ml}$, cells: $1 \times 10^7/\text{ml}$, 200 μl), respectively. We specially designed the control group (P4) for the sake of testing cross-therapy effect on the 545 and 4T1 carcinoma using the CM-EMT6 vaccine. As presented in Fig. 4b, the 545 tumor growth of the CM-545 vaccine therapy group (P0) was significantly inhibited ($p < 0.0001$) in comparison with the control groups (P1-P3) and the Cross-vaccine therapy group (P4) as well. It should be noted that the 545 tumor was not effectively inhibited in the cross-vaccine therapy group (P4), implying an important fact that the anti-tumor response could only be specifically triggered by the CM-cancer vaccine fabricated with the exact same kind of cancer cells. All of the mice in P0 group were tumor-free or without detectable tumor foci after the CM-545 vaccine treatment on the day 40 and no mice died in three months (Fig. 4c). Similar anti-tumor response could also be observed in the therapy group with CM-4T1 vaccine in Balb/c mice with 4T1 tumor, as shown in Fig. 4d and Supplementary Fig. 18. We further conducted flow cytometric analyses using various markers. The data revealed a significant increase of the percentage of activated CD8^+ T cells in the total number of CD8^+ T cells in CM-4T1 tumors compared to CQDs, H-4T1, or PBS groups (Fig. 4e). Analysis of the 4T1 tumor tissues with antibodies for CD8^+ , cleaved caspase-3 and Ki67 further revealed remarkable enhancement of cytotoxic T cells response and apoptosis of cancer cells with significant reduction of proliferation in the CM-4T1 vaccine therapy group of Balb/c mice (Fig. 4f).

To further reveal potentials of the CM-cancer vaccines, we introduced a transgenic mouse model that carried a triple-negative mammary tumor in form of *Fgfr2-S252W* (unpublished data), and designed a personalized therapeutic vaccination protocol, as shown in Extended Data Fig. 2. When the primary mammary tumors in the *Fgfr2-S252W* mice reached at about 500–750 mm^3 in size, a part of the tumors were surgically taken out from the mouse body for producing CM-cancer vaccine. The mice were randomized into two groups: the therapeutic group with injection of the CM-cancer (*Fgfr2-S252W*) vaccine, and the control group with injection of PBS only. In comparison with the control group, the *Fgfr2* tumors in the therapeutic group were significantly inhibited (Extended Data Fig. 2). And the anti-cancer T cell response in the primary tumor site and inhibition of the lung metastasis could also be observed in the

therapeutic group (Extended Data Fig. 2). Above data suggested that CM-cancer vaccines possessed enormous potential on personalized immunotherapeutics.

CM-cancer vaccines for metastatic cancer immunotherapy

4T1 tumor have strong spontaneous metastatic capability⁴¹. In the therapy group with CM-4T1 vaccine in Balb/c mice with 4T1 tumor, the lung metastases of 4T1 tumors were significantly inhibited in contrast with the control groups of P1-P4, as shown in Fig. 4g, 4h. Through comparison of the H&E staining tissue slices of the excised main organs from the five groups, surprisingly we observed that all cancer metastases of the 4T1 carcinoma in organs, including lung, liver and spleen, were perfectly inhibited by the CM-4T1 vaccine therapy, as shown in Fig. 4i, Supplementary Fig. 19. The immunotherapy efficacy of the CM-cancer vaccine for metastatic cancer was further studied in a 4T1 mammary cells transplanted spontaneous metastasis mouse models (Fig. 5a and b). The 4T1 primary tumors were surgically removed out at about 500–750 mm³ in size, and the mice were randomized into the therapy group of (M0) with the CM-4T1 vaccination, and four control groups of (M1) PBS, (M2) pure CQDs, (M3) H-4T1, and (M4) CM-EMT6 vaccine, respectively. In comparison with the H&E staining slices of lung and liver, the number of metastatic nodules in the therapy group (M0) were significantly reduced with the lowest number of macroscopic metastatic nodules among the five groups (Fig. 5c, Supplementary Fig. 20). By checking the characteristic protein expression levels of cytotoxic T cells (CD8⁺), MPs (F4/80), DCs (CD11c) and cytokine (IFN- γ) in lung tissues, we observed that anti-cancer immune response was the highest in the therapy group (M0), indicating feasibility and effectiveness of the personalized CM-cancer vaccines for metastatic cancer immunotherapy (Fig. 5d).

Vaccination using weakened or inactivated forms of microbe has been an effective method in providing active **acquired immunity** to prevent infectious diseases. However, vaccination with inactivated (heat-shocked) cancer cells (H-cancer) has only induced a very limited anti-cancer immune response. The low immunogenicity of the H-cancer vaccine is originated from the fact that most of cancer cells are mutated from normal self-body cells, which contain multiple immune inhibitory proteins with “don’t eat me” signal to prevent phagocytosis by MPs and DCs^{12–15}. In addition, the ratio of potential cancer neoantigen proteins with strong immunogenicity is much smaller than the normal self-proteins, leading to negligible weak “eat me” signal from the neoantigens. Even with current advanced technology, it is still very challenging to custom prepare personalized neoantigen vaccines within days at an affordable cost. All these factors produce the main obstacles in clinical application of cancer-cell-based vaccines⁴². As well-known, the immunogenicity of proteins are greatly dependent on their conformations⁴³. In the proposed CM-cancer vaccine technology, the combination between CQDs and proteins on cancer cells significantly modifies the conformational structures of the proteins, as illustrated in Extended Data Fig. 3. This not only causes dysfunction of the immune inhibitory proteins, but also improve the immunogenicity of the CM normal self-proteins, making significant enhancement in efficiency of cellular-uptaking of CM-cancer by MPs, and up-regulated MHC-II expression. The method reported in this paper has demonstrated that the cytotoxic T-cells response in the lymph nodes is much more robust and efficient. It should be noted

that the 4T1 tumor growth in the CM-EMT6 vaccinated group was not effectively inhibited, implying that the cancer immune response can only be triggered by injecting the CM-cancer fabricated using the same cancer cells. Although both 4T1 and EMT6 are subtypes of breast cancers, they still present their own specific neoantigens. The specific anti-cancer response triggered by the CM-cancer is based on the successful neoantigens presentation with the help of CQDs' modification. In this process, the extremely troublesome and time-consuming neoantigen identification and production are smartly passed to APCs like MPs or DCs. Due to the immunological tolerance of self-body proteins, the CM self-body proteins from the cancer cells engulfed by MPs and DCs would not trigger an over-activated "immune storm" to damage normal self-body tissues under a reasonable injection dose level⁴⁴. In fact, there was no any damages or side effects observed in main organs tissues among the CM-cancer vaccinated mice in our experiments, demonstrating its safety of this method (Supplementary Fig. 19).

In summary, we developed a unique method of thermally combining of cancer cells with CQDs to prepare CM-cancer for personalized cancer immunotherapy. The ultra-small sizes and the abundant biocompatible groups on the CQDs' surface made the CQDs possible to permeate into the proteins and formed enhanced hydrogen bonds with the protein chains under a thermal treatment, then eventually led to irreversible conformational changes of the proteins. Through this thermal induced non-distinctly modification process of proteins by the CQDs, the enhancement in immunogenicity of the CM-cancer vaccines were obvious, as evidenced by a number of mice and zebrafish experiments. The vaccination with CM-cancer efficiently recruited and activated MPs and DCs, then effectively delivered the cancer antigens into the lymph nodes to activate cytotoxic T cells, and finally led to a specific anti-cancer immune response for the whole body to kill primary and metastatic tumors. More importantly, the whole preparation time of the CM-cancer vaccines took only several hours, which provides a distinct and incomparable advantage for customized cancer immunotherapy. Our research reported in this paper intelligently and fruitfully demonstrated a facile, low cost, quick and most importantly very efficient cancer immunotherapy technology. This technology would be acting as a shining light in the area of cancer immunotherapy.

Methods

Synthesis of CQDs

2 g citric acid and 8 g urea were dissolved thoroughly in 30 ml DMSO. The solution and 2 g activated 4A molecular sieve were turned into a reaction autoclave and heated at the temperature of 160 °C for 6 hr under a solvothermal condition. The acquired dark solution was collected and mixed with twice its volume of ethanol solution, then centrifuged at 8000 r min⁻¹ for 5 min to remove residual solvents and eventual organic molecular by-products. The precipitate was dissolved in ultrapure water and purified by dialysis (MWCO = 1000) against ultrapure water for 48 hr. The dialysate was freeze-dried to obtain a dark product of CQDs. Materials: Citric acid, urea and DMSO were purchased from Aladdin, Shanghai.

MD simulation

The initial structure of the CQDs was manually built by Discovery Studio 2016 Client software according to the experimental result of element analysis for the CQDs (**Fig. 1A** and **Fig. 1B**). The GAFF force field⁴⁵ was used for modeling the single-layer quantum dot. The partial atomic charges of the CQDs were obtained using the AM1–BCC charge model⁴⁶. In order to build a multilayer CQDs structure, Packmol⁴⁷ software was used to randomly place all elements together, forming the initial four-layer CQDs structure after 0.5 ns MD simulation (**Fig. 1D**).

The protein structure of BSA was cited from the PDB database (4f5s.pdb), and the ff99SB force field was used to describe the protein structure. This protein was next solvated using the TIP3P⁴⁸ water model in all three dimensions. And then, the system was investigated at two different temperatures: 37 °C and 70 °C, respectively. The whole MD simulation process lasted for 100 ns until reaching a stable conformational structure.

To investigate the interaction between the CQDs and the BSA, the obtained BSA structure was surrounded by three CQDs using Packmol software (BSA+CQDs system at 0 ns). The initial structure was immersed in 10 Å water molecules to form a solvated system. The whole MD simulation process was performed at 37 °C and 70 °C and lasted for 100 ns until reaching a balanced conformation.

All simulations were carried out by the Amber 18 software. The solvated models were subjected to two stages of energy minimization. The first energy minimization (2000 steps) was used to remove bad atom contacts in water molecules. And the second energy minimization (20000 steps) was performed for the whole system. Next, the solvated model was heated to the required temperature in 20 ps. The temperature was controlled by the Langevin equilibration scheme. After the heating process, MD simulation was performed in the NPT ensemble with periodic boundary conditions. During the simulation process, the SHAKE algorithm was applied to constrain the bond length and angles for water atoms. The detailed simulation protocols were similar to our previous studies^{49,50}.

Reagents and Cell Culture

The murine melanoma cell line B16F10 was purchased from ATCC (Manassas, VA). The B16F10-C3 cell line was generated by transfecting the plasmid DNA of a CFP/YFP FRET-based sensor C3 into B16-F10 cells and isolated from a single clone, which could detect the caspase-3 (C3) activation based apoptotic^{51,52}. These cells were maintained in Dulbecco's modified Eagle medium (DMEM; GIBCO, Los Angeles, CA) supplemented with 10% fetal bovine serum (FBS; HyClone, Logan, UT) and 1% penicillin and streptomycin at 37°C with 5% CO₂. The 1,1'-dioctadecyl-3,3,3',3'-tetramethylindocarbocyanine perchlorate (DiI; Invitrogen, Carlsbad, CA, USA) were used to label B16F10 with red fluorescence according to manufacturer's protocol.

Potential biotoxicity and fluorescence imaging of CQDs

The environment contains 5% CO₂ (the temperature is 37 °C). MDA-MB-231 cells were cultured in Dulbecco's modified Eagle medium with 10% fetal bovine serum and 1% penicillin/streptomycin. 4T1 cells

and EMT6 cells were cultured in ATCC-formulated RPMI-1640 Medium with 10% fetal bovine serum and 1% penicillin/streptomycin. And the 3-[4,5-dimethylthiazol-2-yl]-2,5-diphenyltetrazolium bromide (MTT) assays were used for in vitro cell activities evaluation. These cells were seeded into U-bottom 96-well cell culture plates. The density of cells was 5×10^4 well⁻¹.

Then, the media were removed and these cells in wells were incubated with CQDs aqueous solution at various concentrations (0–1mg/ml) at 37 °C for 48 h. After 48 h the MTT (20 µl, 5mg/ml) was added and cells were incubated in the each well for 4 h. Absorbance (OD570 nm) of each well was measured by microplate reader and the cell viability was calculated via the following equation (A_t is the mean absorbance value of the treatment group and A_c is the mean absorbance value of the control group):

$$\text{Cell Viability} = \frac{A_t}{A_c} \times 100 \% \quad (\text{Equation 1})$$

For cell viability detection after exposure to the laser, the cells were costained with a live/dead cell double staining kit to monitor viable and dead cells with the confocal fluorescence microscope. The double staining kit contained acetoxymethyl ester of calcein which stained only viable cells with green fluorescence, and propidium iodide which stained only dead cells with red fluorescence.

Fluorescence imaging of CQDs

The environment contains 5% CO₂ (the temperature is 37 °C). MDA-MB-231 cells were cultured in Dulbecco's modified Eagle medium with 10% fetal bovine serum and 1% penicillin/streptomycin. 4T1 cells and EMT6 cells were cultured in ATCC-formulated RPMI-1640 Medium with 10% fetal bovine serum and 1% penicillin/streptomycin. These cells were seeded into U-bottom 12-well cell culture plates. After the cell density in the well has grown to 80%, add a solution of near-infrared CQDs with a concentration of 50 µg/ml. After culturing for 24 hours, place one well plate into a oven at 50 °C for 10 min, and the other is left untreated. The experimental group and the control group of the cell photothermal experiment were obtained respectively. Finally, the two groups of cells were placed under a laser scanning confocal microscope (Nikon Ti2 microscope) or fluorescence microscope (Axio Observer: Z1/7) for fluorescence imaging and analysis of the cells. Ex 533-558 nm/Em 570-640 nm.

All animal experiments were conducted according to the animal research guidelines provided by the Animal Care and Use Committee at the University of Macau.

Fluorescence images of mice major organs and whole body were acquired using using an ORCA-Flash4.0 V2 Digital CMOS camera. The excitation laser (655 nm) was generated from cnilaser MD-655NM-HS-2W16060512 (10.6 mW cm⁻²) and emitted light was further filtered through a 700-nm longpass filter that was coupled to the CMOS camera. The exposure time is 400 ms, and the images were further processed with the ImageJ image analysis software.

Cellular experiment and flow Cytometry

RAW 264.7 cells were seeded in 24-well plates at a density of 1×10^5 cells per well and grown in an incubator at 37 °C with 5% CO₂ for 1 day. After removing the culture medium, the cells were exposed to the 0.5 ml of the PBS, CQDs (50 ug/ml), heat-shocked cancer cells (1×10^7 /ml) and CM-cancer vaccine for 6 hr (CQDs: 50 ug/ml, Cells: 1×10^7 /ml). Then, the cells were washed and trypsinized to obtain single-cell suspension. The cells in each well were incubated with 5% bovine serum albumin (BSA) in PBS at 4 °C for 15 min. The samples were incubated with phycoerythrin-conjugated rat anti-mouse MHC class II (PE anti-mouse MHC II) or phycoerythrin-conjugated rat IgG2a isotype control (PE anti-mouse IgG2a ISO) for 30 min at 4 °C. Samples were washed by PBS and run on BD LSRFortessa™ (Becton, Dickinson and Company, Franklin Lakes, NJ, USA). The results were analyzed by FlowJo software (Tree Star Inc., Ashland, OR, USA).

Zebrafish Breeding and Culture

All zebrafish experiments were approved by the Institutional Animal Care and Use Committees of University of Macau. Zebrafish (*Danio rerio*) were maintained at standard conditions and guidelines in accordance with the Zebrafish Model Organism Database (<http://zfin.org>). The A/B wild type and transgenic zebrafish lines *Tg(mpeg1:EGFP)* and *Tg(lck:EGFP)* who expressed EGFP in macrophages and T cells were used in the following studies. Adult fish were fed twice a day with newly hatched shrimp and raised in an aquaculture system with 12 hr alternating light/dark cycles. Eggs from adult zebrafish were collected and kept in zebrafish culture media at 28 °C. In order to suppress pigment cell formation, 0.003 wt% 1-phenyl 2-thiourea (PTU) was contained in the culture media 1-day post fertilization (dpf).

Macrophage Activation in *Tg(mpeg1:EGFP)* Transgenic Zebrafish Model

To investigate the interaction between CM-cancer vaccines and macrophages, 4 nl PBS, CQDs, heat-shocked cancer cells and CM-cancer vaccine were intraperitoneally injected into 6 dpf *Tg(mpeg1:EGFP)* transgenic zebrafish larvae. At 6- and 24- hour post injection (dpi), the zebrafish larval were anesthetized with 0.01% tricaine and positioned on a wet agarose in a living cells dish, then imaged under a Leica SP8 CLSM equipped with a 20× air objective. The fluorescence images were acquired at Ex 488 nm/Em 493–550 nm for EGFP signal and Ex 552 nm/Em 558 – 650 nm for CQDs or Dil signal detection under the independent sequence of channel with HyD detectors.

Established Cancer Xenograft Zebrafish Model

The Dil labelled B16F10 or B16F10-C3 cells line were microinjected into zebrafish to generate xenograft cancers⁵³ Briefly, the cancer cells were collected by trypsinization and centrifuged for 3 min at 1,000 rpm. The cell pellet was washed twice with PBS and resuspended in 50 µl of PBS at a concentration of 1×10^6 cells/50 µl and placed on ice for microinjection. Using a 10 µl pipette, the highly concentrated cells were loaded into the glass micropipette and subsequently fixed onto the Nanoject \square Injector (Drummond Scientific Company, USA). At 48 hpf, zebrafish larvae were anesthetized and positioned on a wet agarose microinjection pad. Cell suspension (5 nl) containing 100 cancer cells was injected into A/B wild type, *Tg(mpeg1:EGFP)* and *Tg(lck:EGFP)* transgenic zebrafish embryo (2 dpf) beneath the yolk sac. After

microinjection, zebrafish embryos were maintained in a 32 °C incubator. At 2–day post injection (dpi), the injected zebrafish embryos were observed using stereo fluorescence microscope SMZ18 (Nikon, Japan) to exclude unsuccessfully transplanted zebrafish.

Immunity Activation in Cancer Xenograft Zebrafish Model

To investigate the immunity activation process of CM-cancer against cancer in zebrafish model, 4 nl PBS and CM-cancer vaccine were intraperitoneally injected into 3–day Dil labelled B16F10 cancer xenograft Tg(*mpeg1:EGFP*) and Tg(*Ick:EGFP*) transgenic zebrafish model. On the 2nd, 3rd, 4th, 5th and 6th day post cancer xenograft, the zebrafish larval were anesthetized with 0.01% tricaine and positioned on a wet agarose in a living cells dish, then imaged under a Leica SP8 CLSM equipped with a 20× air objective to visualize the status of cancer, macrophages and T cells in zebrafish. The fluorescence images were acquired at Ex 488 nm/Em 493–550 nm for EGFP signal and Ex 552 nm/Em 558–650 nm for Dil signal detection under the independent sequence of channel with HyD detectors.

Evaluation of Anti–cancer effect in zebrafish model

To evaluate the anti–cancer effect of CM-cancer vaccine in zebrafish, 4 nl PBS, CQDs, heat-shocked cancer cells and CM-cancer vaccine were intraperitoneally injected into the 3–day B16F10-C3 cancer xenograft A/B wild type zebrafish model. On the 2nd, 3rd, 4th, 5th, 6th and 8th day post cancer xenograft, the zebrafish larval were positioned on a wet agarose in a living cells dish, then imaged under a stereo fluorescence microscope SMZ18 (Nikon, Japan) with GFP channel to observe the cancer growth. The cancers of zebrafish larval were quantified by measuring the long diameter *a* and short diameter *b* of cancer in fluorescent images. Then, the cancer volume *V* was estimated using the equation $V = (ab^2)/2$.⁹ To detect the apoptosis of single cells in zebrafish xenograft cancer, FRET imaging was acquired at Ex 448 nm/Em 450–500 nm for CFP signal and Em 520–550 nm for YFP signal detection under a Leica SP8 CLSM equipped with a 20× air objective at 3 and 6–day post cancer xenograft.

Animals

All animal experiments were approved by the University of Macau Animal Ethics Committee under the protocol (UMAEC-037-2015). *Fgfr2*^{Neo-S252W/+;MMTV-Cre} (*Fgfr2-S252W*) mice were generated by breeding *Fgfr2*^{Neo-S252W/+} mice (Chen et al., 2003b), which were further interCrossed with *MMTV-Cre* mice to generate *Fgfr2-S252W* mice.

Whole Mounts, H&E, Immunohistochemistry staining

The fourth abdominal mammary glands were harvested from pubertal mice, placed between two glass slides, and spread by placing weights on top of the slides, followed by fixing in EtOH: CHCl₃: HOAc (6:3:1, v/v) using the methods described previously. The mammary glands were fixed with 4% Paraformaldehyde, and then stained with correspondent antibodies using methods described previously. Deparaffinized sections from mammary glands were cooked with Retriever (Electronic Microscopy

Science, 62700-10) in Buffer A (citrate buffer, pH 6.0) followed by staining with antibody. Images were acquired using Nikon A1R Confocal System or Olympus IX83 Inverted Microscope. Antibodies for Immunohistochemistry / Immuno-fluorescence staining are listed on Supplementary Table 1.

Tumor Digestion

Tumor cells were isolated, finely minced, and digested with Digestion I at 37 °C for 3-4 hr. After cells were spun down, they were treated with Digestion II for 5 min. Digested tumor cells were washed with Hanks solution and lysed with red blood cell (RBC) Lysis Solution. Cells were resuspended in Flow Cytometry Staining Buffer (ThermoFisher Scientific) and incubated with antibodies (Supplementary Table 2) for 1 hr on ice. Then, the cells were washed and resuspended by Flow Cytometry Staining Buffer and analyzed by flow cytometry (BD FACSAria III). Signal threshold definition was defined using all-stained, unstained and isotype controls.

Declarations

Acknowledgments

The authors wish to acknowledge Prof. Ming Yuen Lee for providing *Tg(lck:EGFP)* transgenic zebrafish, and the Animal Facility of the Faculty of Health Sciences, University of Macau for providing the animal housing.

Fundings

National Natural Science Foundation of China 61922091. Science and Technology. Development Fund (Macau) 0040/2019/A1, 0011/2019/AKP, 0015/2018/A1. Research and Development Grant for Chair Professor Fund from the University of Macau CPG2020-00026-IAPME, CPG2021-00034-IAPME, CPG2021-00021-FHS. Research Grant from the University of Macau MYRG2019-00103-IAPME, SRG2019-00163-IAPME, MYRG2017-00200-ICMS.

Author contributions

Z. K. Tang led and designed the whole project, and involved every steps of the investigation. S. N. Qu discovered the CQD-based anti-cancer immunotherapy phenomena, and participated the whole project investigations. C. X. Deng led the part of biomedicine study and designed cancer immunotherapy using various mouse models. T. Liang focused the CQDs synthesis and participated all investigations including the biomedicine experiments. H. P. Lei focused the biomedicine and conducted experiments for cancer treatment and immunotherapy using various mice models. S. Guo participated experiments for cancer treatment and immunotherapy using various mouse models. Y. Zheng together with J. S. Tao contributed the zebrafish experiments. W. Ge offered *Tg(mpeg1:EGFP)* transgenic zebrafish model and guidance for zebrafish experiments. Q. Luo provided *B16F10-C* transgenic zebrafish model. D. F. Ouyang together with H. L. Gao performed the MD simulation of CQDs and BSA complexation.

Competing interests

Authors declare that they have no competing interests.

Data and materials availability

All data are available in the main text or the supplementary materials

References

1. Cahill, D. P. et al. Mutations of mitotic checkpoint genes in human cancers. *Nature* **392**, 300–303(1998).
2. Hofree, M. et al. Network-based stratification of tumor mutations. *Methods* **10**, 1108–1115(2013).
3. Mellman, I., Coukos, G. & Dranoff, G. Cancer immunotherapy comes of age. *Nature* **480**, 480–489 (2011).
4. Sahin, U. & Türeci, Ö. Personalized vaccines for cancer immunotherapy. *Science* **359**, 1355–1360 (2018).
5. Ott, P. A. et al. An immunogenic personal neoantigen vaccine for patients with melanoma. *Nature* **547**, 217–221(2017).
6. Bulik–Sullivan, B. et al. Deep learning using tumor HLA peptide mass spectrometry datasets improves neoantigen identification. *Biotech.* **37**, 55–63(2019).
7. Khodadoust, M. S. et al. Antigen presentation profiling reveals recognition of lymphoma immunoglobulin neoantigens. *Nature* **543**, 723–727(2017).
8. Sahin, U. et al. Personalized RNA mutanome vaccines mobilize poly–specific therapeutic immunity against cancer. *Nature* **547**, 222–226 (2017).
9. Gong, N. et al. Proton–driven transformable nanovaccine for cancer immunotherapy. *Nanotech.* **15**, 1053–1064 (2020).
10. Damo, M. et al. Inducible de novo expression of neoantigens in tumor cells and mice. *Biotech.* **39**, 64–73(2021).
11. Van der Burg, S. H. et al. Vaccines for established cancer: overcoming the challenges posed by immune evasion. *Rev. Cancer* **16**, 219–233 (2016).
12. Bradley, C. A. CD24—a novel ‘don’t eat me’signal. *Rev. Cancer* **19**, 541–541(2019).
13. Elward, K. & Gasque, P. “Eat me” and “don’t eat me” signals govern the innate immune response and tissue repair in the CNS: emphasis on the critical role of the complement system. *Immunol.* **40**, 85–94(2003).
14. Paidassi, H. et al. How phagocytes track down and respond to apoptotic cells. *Rev. Immunol.* **29**, 111–130 (2009).
15. Czaja, A. J. Immune inhibitory proteins and their pathogenic and therapeutic implications in autoimmunity and autoimmune hepatitis. *Autoimmunity* **52**, 144–160 (2019).

16. Shrestha, A. C. et al. Cytolytic perforin as an adjuvant to enhance the immunogenicity of DNA vaccines. *Vaccines* **7**, 38(2019).
17. Zhang, Y. N. et al. Nanoparticle size influences antigen retention and presentation in lymph node follicles for humoral immunity. *Nano Lett.* **19**: 7226–7235(2019).
18. Lynn, G. M. et al. In vivo characterization of the physicochemical properties of polymer–linked TLR agonists that enhance vaccine immunogenicity. *Biotech.* **33**, 1201–1210(2015).
19. Pardoll, D. M. The blockade of immune checkpoints in cancer immunotherapy. *Rev. Cancer* **12**, 252–264(2012).
20. Ribas, A. & Wolchok, J. D. Cancer immunotherapy using checkpoint blockade. *Science* **359**, 1350–1355 (2018).
21. Han, X. et al. Red blood cell–derived nanoerythroosome for antigen delivery with enhanced cancer immunotherapy. *Adv.* **5**, eaaw6870 (2019).
22. Patel, S. A. & Minn, A. J. Combination cancer therapy with immune checkpoint blockade: Mechanisms and strategies. *Immunity* **48**, 417–433 (2018).
23. Bao, X. et al. In vivo theranostics with near–infrared–emitting carbon dots—highly efficient photothermal therapy based on passive targeting after intravenous administration. *Light Sci. Appl.* 1–11(2018).
24. Liu, C. et al. Nano–carrier for gene delivery and bioimaging based on carbon dots with pei–passivation enhanced fluorescence. *Biomaterials* **33**, 3604–3613 (2012).
25. Li, S. et al. Targeted tumour theranostics in mice via carbon quantum dots structurally mimicking large amino acids. *Biomed. Eng.* **4**, 704–716 (2020).
26. Liang, T. et al. Morphology Control of Luminescent Carbon Nanomaterials: From Dots to Rolls and Belts. *ACS nano* (2020).
27. Liu, E. et al. Enhanced Near–Infrared Emission from Carbon Dots by Surface Deprotonation. *Phys. Chem. Lett.* **12**, 604–611(2020).
28. Damodaran, S. In situ measurement of conformational changes in proteins at liquid interfaces by circular dichroism spectroscopy. *Bioanal. Chem.* **376**, 182–188(2003).
29. Palucka, K. & Banchereau, J. Cancer immunotherapy via dendritic cells. *Rev. Cancer* **12**, 265–277(2012).
30. Jaynes, J. M. et al. Mannose receptor (CD206) activation in tumor–associated macrophages enhances adaptive and innate antitumor immune responses. *Transl. Med.* **12**, (2020).
31. Nizet, V. & Johnson, R. S. Interdependence of hypoxic and innate immune responses. *Rev. Immunol.* **9**, 609–617(2009).
32. Shen, L. H. et al. Oxidized low–density lipoprotein induces differentiation of RAW264. 7 murine macrophage cell line into dendritic–like cells. *Atherosclerosis* **199**, 257–264(2008).
33. He, X. et al. Visualization of human T lymphocyte–mediated eradication of cancer cells in vivo. *Proc. Acad. Sci. U. S. A.* **117**, 22910–22919(2020).

34. Tao, J. et al. Toward understanding the prolonged circulation and elimination mechanism of Crosslinked polymeric micelles in zebrafish model. *Biomaterials* **256**, 120180(2020).
35. Ellett, F. et al. *mpeg1* promoter transgenes direct macrophage-lineage expression in zebrafish. *Blood* **117**E49–E56(2011).
36. Sanderson, L. E. et al. An inducible transgene reports activation of macrophages in live zebrafish larvae. *Comp. Immunol.* **53**, 63-69(2015).
37. Okuda, K. S. et al. lyve1 expression reveals novel lymphatic vessels and new mechanisms for lymphatic vessel development in zebrafish. *Development* **139**, 2381–2391(2012).
38. Langenau, D. M. et al. In vivo tracking of T cell development, ablation, and engraftment in transgenic zebrafish. *Natl. Acad. Sci. U. S. A.* 2004, **101**: 7369–7374(2004).
39. Luo, K. Q. et al. Application of the fluorescence resonance energy transfer method for studying the dynamics of caspase-3 activation during UV-induced apoptosis in living HeLa cells. *Biophys. Res. Commun.* **283**, 1054–1060(2001).
40. Fu, A. et al. Rapid identification of antimicrometastases drugs using integrated model systems with two dimensional monolayer, three dimensional spheroids, and zebrafish xenotransplantation tumors. *Bioeng.* **115**, 2828-2843(2018).
41. Yang, L. et al. Disease progression model of 4T1 metastatic breast cancer. *J Pharmacokinet Pharmacodyn* 47, 105–116 (2020)
42. Blass, E. & Ott, P A. Advances in the development of personalized neoantigen-based therapeutic cancer vaccines. *Rev. Clin. Oncol.* **2021**, 1–15 (2021).
43. Scheibelhofer, S., Laimer, J., Machado, Y., Weiss, R. & Thalhamer Influence of protein fold stability on immunogenicity and its implications for vaccine design. *Expert Rev Vaccines.* **16**, 479–489(2017).
44. Klein, L., Robey, E. A. & Hsieh, C. S. Central CD4+ T cell tolerance: deletion versus regulatory T cell differentiation. *Rev. Immunol.* **19**, 7–18 (2019).
45. Wang, J. et al. Development and testing of a general amber force field. *J. Comput. Chem.* **25**, 1157–1174(2004).
46. Jakalian, A., Jack, D. B. & Bayly, C. I. Fast, efficient generation of high-quality atomic charges. AM1–BCC model: II. Parameterization and validation. *J. Comput. Chem.* **23**, 1623–1641(2002).
47. Martínez, L. et al. PACKMOL: a package for building initial configurations for molecular dynamics simulations. *J. Comput. Chem.* **30**, 2157–2164(2009).
48. Price, D. J. & Brooks, C. L. A modified TIP3P water potential for simulation with Ewald summation. *J. Chem. Phys.* **121**, 10096–10103(2004).
49. Han, R. et al. Predicting physical stability of solid dispersions by machine learning techniques. *J. Control. Release* **311–312**, 16–25(2009).
50. Chan, T.& Ouyang, D. Investigating the molecular dissolution process of binary solid dispersions by molecular dynamics simulations. *Asian J. Pharm.* **13**, 248–254(2018).

51. Luo, K. Q. et al. Application of the fluorescence resonance energy transfer method for studying the dynamics of caspase-3 activation during UV-induced apoptosis in living HeLa cells. *Biochem. Biophys. Res. Commun.* **283**, 1054–1060(2001).
52. Fu, A. et al. Rapid identification of antimetastases drugs using integrated model systems with two dimensional monolayer, three dimensional spheroids, and zebrafish xenotransplantation tumors. *Biotechnology and Bioengineering* **115**, 2828–2843(2018).
53. Deng, S. et al. Biodegradable polymeric micelle-encapsulated doxorubicin suppresses tumor metastasis by killing circulating tumor cells. *Nanoscale*, **7**, 5270–80(2015).

Figures

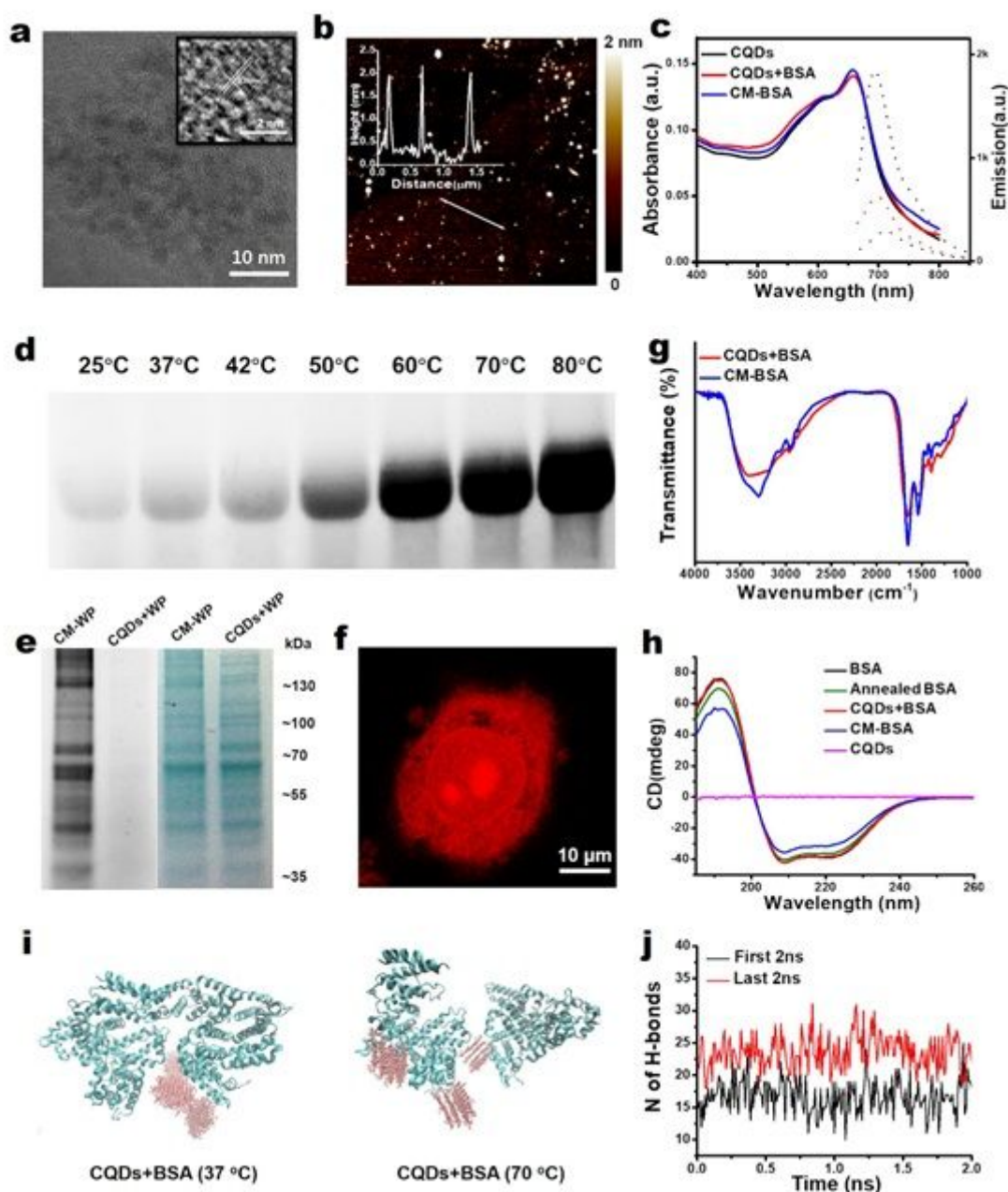


Figure 1

Design and characterization of CQDs, CM-BSA and CM-cancer. (a) TEM image of CQDs; inset: HRTEM image of a CQD; (b) AFM image of CQDs; inset: height distribution of the CQDs; (c) Absorption (solid lines) and emission (dotted lines, excitation at 655 nm) spectra of the aqueous solutions of CQDs, CQDs+BSA and CM-BSA, respectively. BSA and CQDs concentrations in the solutions are 50 $\mu\text{g/ml}$ and 10 $\mu\text{g/ml}$, respectively; (d) Fluorescence (excitation: 647 nm, filter: 700 nm) images of SDS-PAGE pattern of BSA with CQDs after thermal annealing at different temperatures; (e) Fluorescence (excitation: 647 nm, filter: 700 nm) (left) and Coomassie brilliant blue staining (right) images of SDS-PAGE pattern of Fgfr2-S252W tumors whole proteins with CQDs after annealing (CM-WP) and without annealing (CQDs+WP), respectively; (f) CLSM image of a single CM-4T1 (excitation: 632 nm, filter: 700 nm); (g) FTIR spectra of CQDs+BSA and CM-BSA freeze-dried powders; (h) CD spectra of CQDs, BSA, CQDs+BSA and CM-BSA aqueous solutions at room temperature. BSA and CQDs concentrations in the solutions are 50 $\mu\text{g/ml}$ and 10 $\mu\text{g/ml}$, respectively; (i) Simulational configurations of the BSA molecule with CQDs in aqueous solution at 37 oC and 70 oC after 100 ns simulation. Water molecules are not shown. CQDs and BSA are presented in brown and green, respectively; (j) The number (N) of hydrogen bonds between BSA and CQDs at 70 oC in the first 2 ns (black) and last 2 ns (red) during 100 ns simulation.

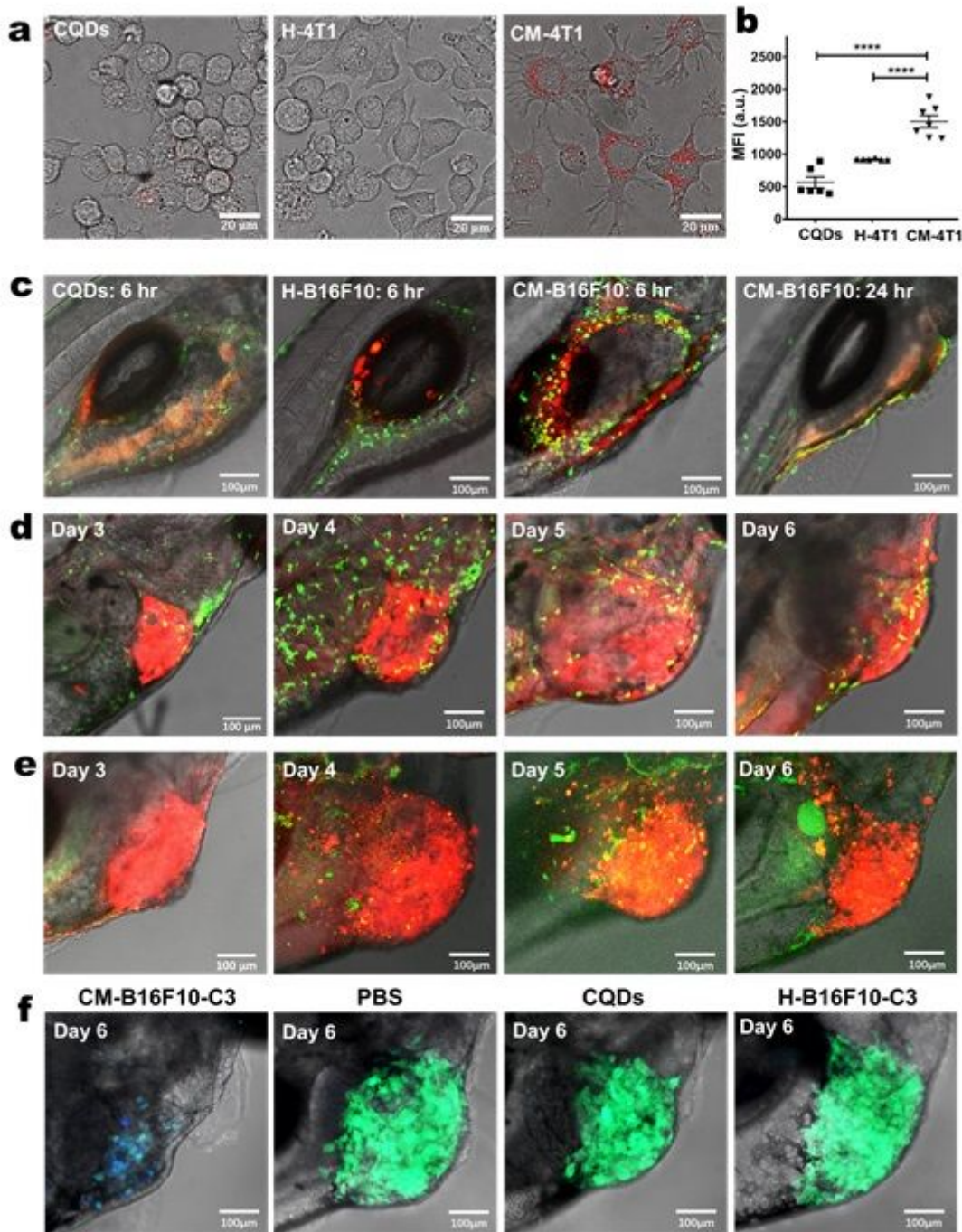


Figure 2

CM-cancer induced hyperactivation of MPs and anti-cancer immune response in zebrafish model. (a) CLSM images of the MPs, from left to right : after co-incubating with CQDs, H-4T1 and CM-4T1, respectively; (b) MHC-II marked fluorescence intensities (MFI) from the MP cells in different treating groups; data were collected using a flow cytometer after the MPs were cultured in vitro with H-4T1 ($n = 6$), CQDs ($n = 6$) and CM-4T1 ($n = 7$), respectively, for 24 hr. $p < 0.0001$ (****). CQDs: 50 $\mu\text{g}/\text{ml}$, 4T1 cells: $1 \times 10^7/\text{ml}$, respectively. Data plotted are mean \pm S.E.M; (c) From left to right, CLSM images of MPs (Green) response in Tg(mpeg1:EGFP) transgenic zebrafish model after abdominal injection with CQDs (Red), Dil dyes labeled H-B16F10 (Red) and CM-B16F10 (Red), respectively, at equivalent dose at 4 nl for 6

hr and 24 hr; CQDs: 200 µg/ml, B16F10 cells: 1×10⁷/ml, 4 nl; (d) CLSM images of the MPs response in Dil labelled B16F10 cancer xenograft Tg(mpeg1:EGFP) zebrafish model treated with CM-B16F10; MPs (Green), B16F10 cells (Red); (e) CLSM images of the anti-cancer T cells response in Dil labelled B16F10 cancer xenograft Tg(lck:EGFP) zebrafish model treated with CM-B16F10, T cells (Green), B16F10 cells (Red); (f) CLSM images of monitoring the cancer cell proliferation growth (Green) and detect the caspase-3 activation based apoptotic (Blue) by FRET imaging in B16F10-C3 cancer xenograft zebrafish model after PBS, CQDs, H-B16F10-C3 and CM-B16F10-C3 treatments at day 6, respectively.

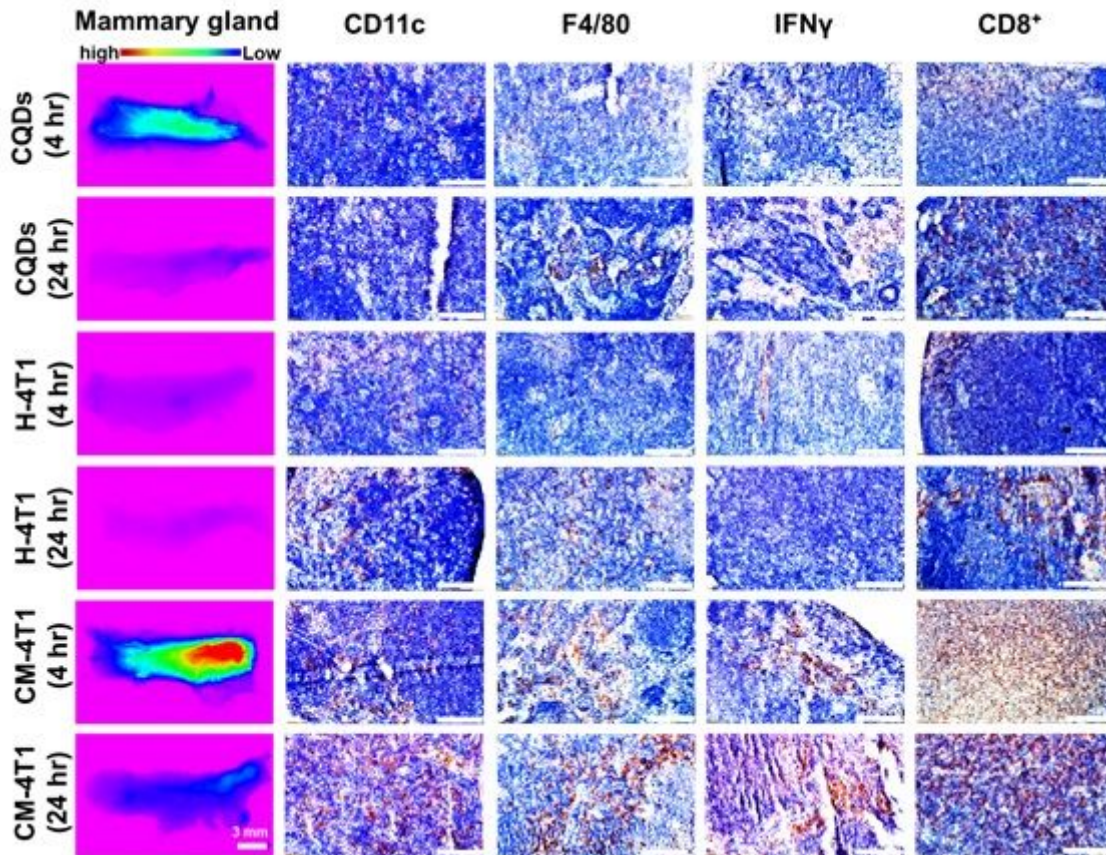


Figure 3

The CM-cancer vaccine generates robust immune responses in lymph node. Fluorescent images of the 4th mammary tissue with inguinal lymph node (left) after abdominal injection with CQDs, H-4T1 labeled with fluorescent dyes (DID 700) and CM-4T1, respectively, at equivalent dose (200 µl per mice) at 4 hr and 24 hr (Scale bar: 3 mm), 647 nm excitation (BA 700 nm). IHC staining of the lymph nodes against CD11c, F4/80, IFN γ , and CD8⁺ with indicated treatment groups (Scale bar: 100 µm).

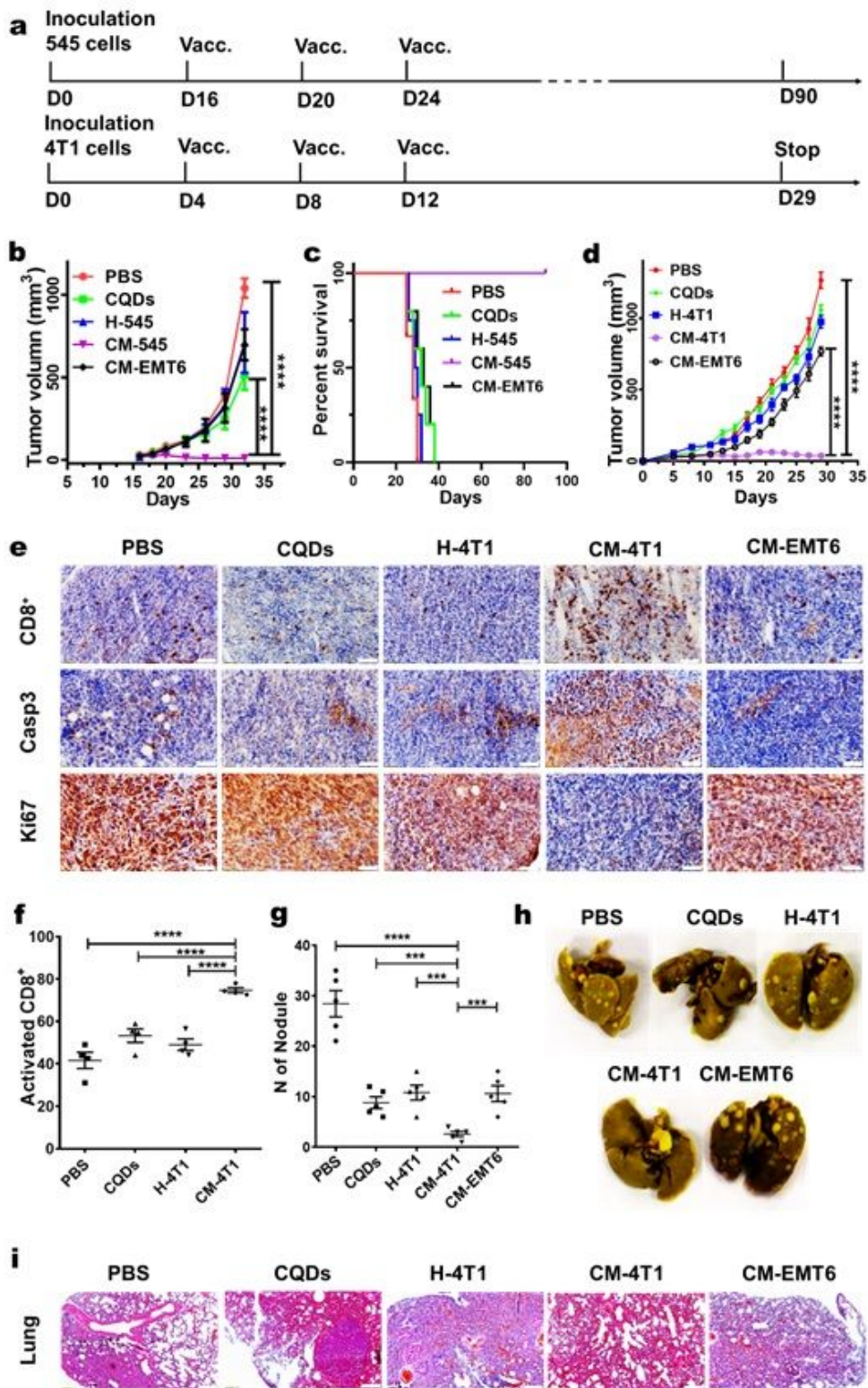


Figure 4

CM-cancer vaccine inhibits tumor growth and metastasis on murine mammary cancer models. (a) Schematic illustration of CM-545 and CM-4T1 vaccines to inhibit primary 545 tumor in FVB and 4T1 tumor in Balb/c murine mammary model, respectively; (b) Growth curves of 545 tumors and c, percent survival of FVB murine treated with CM-545 (n = 6), CM-EMT6 (n = 5), H-545 (n = 5), PBS (n = 5) and CQDs (n = 5), $p < 0.0001$ (****). Data plotted are mean \pm S.E.M.; (d) Growth curves of 4T1 tumors in mice

treated with CM-4T1 (n = 6), CM-EMT6 (n = 6), H-4T1 (n = 6), PBS (n = 6) and CQDs (n = 6), $p < 0.0001$ (****). Data plotted are mean \pm S.E.M; (e) IHC staining of tumor sections from orthotopic transplantation model showing that the CM-4T1 vaccines treatment suppressed the expression of CD8+, Ki67 and induced Cleaved Casp3. Scale bar: 50 μ m; (f) Representative flow cytometry ratios of activated CD8+ T cells in the tumors from different groups after CM-4T1, CQDs, H-4T1 and PBS treatments (n = 4), respectively. $p < 0.0001$ (****). Data plotted are mean \pm S.E.M; (g) Statistics, and (h) images of metastatic tumors in lungs from P0-4 groups after PBS, CQDs, H-4T1, CM-EMT6 and CM-4T1 treatments (n = 5), respectively. $p < 0.0001$ (****), $p = 0.0007$ (***), $p = 0.0004$ (***), $p = 0.0008$ (***). Data plotted are mean \pm S.E.M; (i) H&E staining of lungs from P0-4 groups of 4T1 murine mammary model mice. Scale bar: 200 μ m.

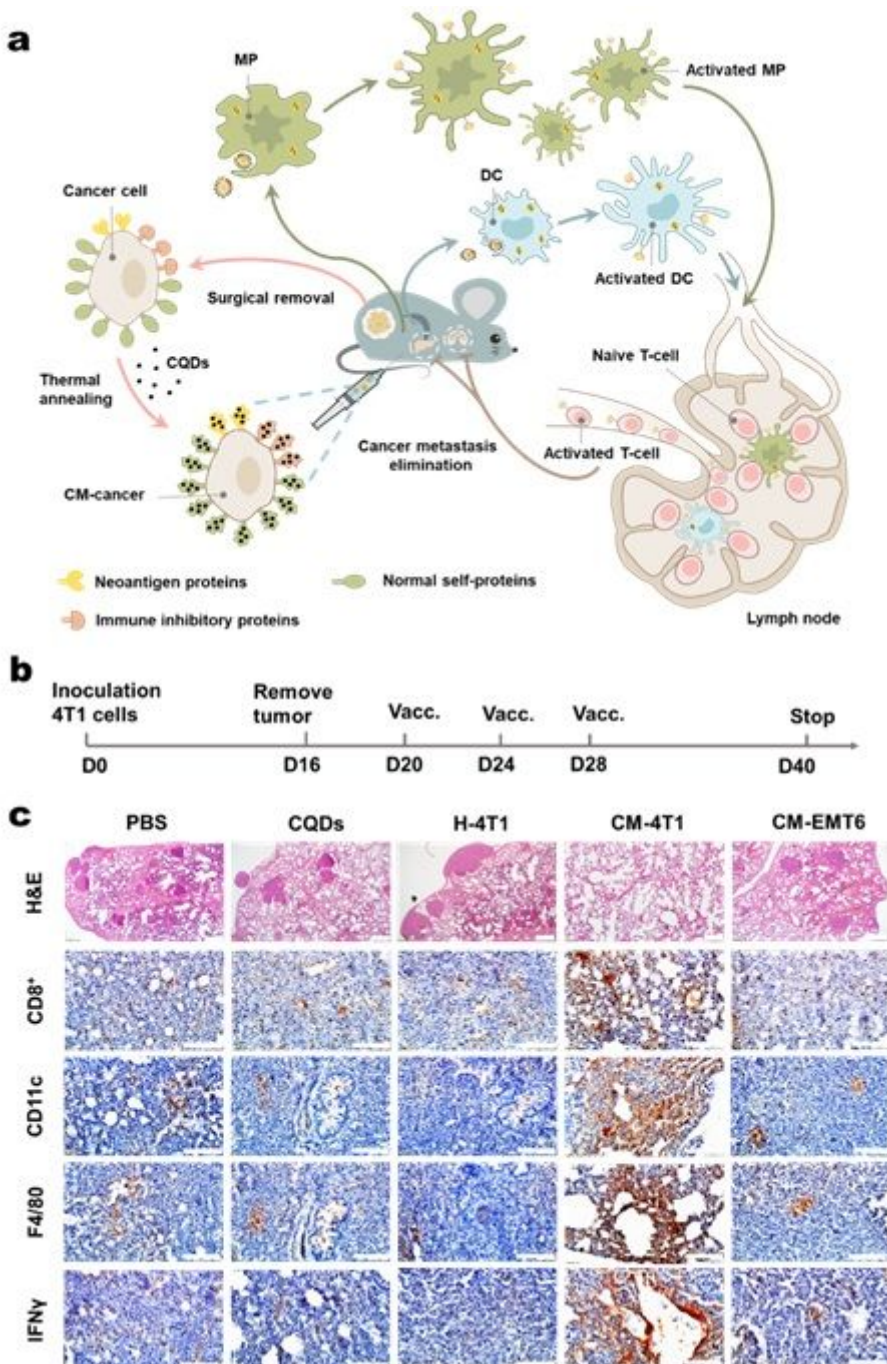


Figure 5

CM-4T1 vaccine cures metastatic cancer on a postoperative 4T1 murine mammary model. (a) Schematic illustration of metastatic cancer immunotherapy on 4T1 murine by the CM-4T1 vaccine. The 4T1 cells was acquired by digesting the primary 4T1 tumor tissue of the mice and thermally combined with CQDs in vitro; (b) Schematic illustration of CM-4T1 vaccine treating the post-surgical 4T1 murine mammary model; (c) H&E and IHC staining of lung tissues from M0-M4 groups after PBS, CQDs, H-4T1, CM-EMT6 and CM-4T1 treatments, respectively. Scale bar: 100 μ m.

Supplementary Files

This is a list of supplementary files associated with this preprint. Click to download.

- [NatureSupplementaryinfo20210423.pdf](#)
- [ExtendedDataFigures.pdf](#)